Carbon Trends 9 (2022) 100210

Contents lists available at ScienceDirect

Carbon Trends

journal homepage: www.elsevier.com/locate/cartre

Shear exfoliated few-layer graphene and cellulose nanocrystal composite as biocompatible anode with efficient charge transfer

Sara Lund[a,b,c], Elisabeth Björnvik[a,b], Qingbo Wang[b,d], Xiaoju Wang[b,d], Sindhujaa Vajravel[c], Laura T. Wey[c], Yagut Allahverdiyeva[c], Jussi Kauppila[a], Jan-Henrik Smått[a], Jouko Peltonen[a], Rose-Marie Latonen[a,b], Tom Lindfors[a,b,*]

[a] Åbo Akademi University, Faculty of Science and Engineering, Laboratory of Molecular Science and Engineering, Henriksgatan 2, 20500 Turku (Åbo), Finland
[b] Åbo Akademi University, Johan Gadolin Process Chemistry Centre (PCC), Henriksgatan 2, 20500 Turku (Åbo), Finland
[c] University of Turku, Department of Life Technologies, Molecular Plant Biology, 20014 Turku, Finland
[d] Åbo Akademi University, Faculty of Science and Engineering, Laboratory of Natural Materials Technology, Henriksgatan 2, 20500 Turku (Åbo), Finland

ARTICLE INFO

Article history:
Received 28 August 2022
Accepted 29 August 2022

Keywords:
natural flake graphite
few-layer graphene
nanocellulose
liquid-phase exfoliation
electroactivity
cytocompatibility

ABSTRACT

Electroconductive composites of graphene and cellulose nanocrystals (CNC) were prepared by direct exfoliation of natural flake graphite in CNC suspensions. Using the scalable high-shear exfoliation method, we show that the environmentally friendly CNC is an excellent graphene stabilizer as we prepared aqueous graphene-CNC dispersions with a high concentration (4.0 mg ml^{-1}) and yield (4.0%) after only 2 h exfoliation time. With this fast and facile method, we exfoliated graphite using CNC with different amounts of negatively charged sulfate ester groups. We found that the graphene concentration is proportional to zeta potential of the CNC suspension suggesting that electrostatic repulsion plays a key role in graphene stabilization. Albeit the insulating nature of CNC, the spray-coated composite films were electrically conductive with conductivity up to 280 S m^{-1}, depending on the CNC amount. Cyclic voltammetry measurements showed a reversible redox response for the $Fe(CN)_6^{3-/4-}$ couple proving that the electron transfer was efficient in the composite film. Furthermore, biocompatibility studies with photosynthetic microorganisms revealed no toxic effects as the cells maintained their photosynthetic performance and growth when placed in direct contact with the composite. The cytocompatibility, electroactivity and good water-stability make the composite film a promising anode for bioelectrochemical applications.

1. Introduction

Due to its many exceptional properties, graphene has become one of the most studied nanomaterials. Graphene can be produced by a variety of different techniques such as micromechanical cleavage (also known as the Scotch-tape method) [1], chemical vapor deposition [2,3], and liquid-phase exfoliation (LPE) of graphite [4–6]. The LPE methods have raised a special interest since in contrast to dispersions of graphene oxide (GO) and reduced graphene oxide (rGO) [7–9], they produce dispersions of defect-free and unoxidized mono- and few-layer graphene [5,6,10] which can be introduced into various processes such as blending, casting or functionalization. For example, processing from liquids enables the formation of thin or free-standing films, mixing with other nanomaterials to form composites and insertion into polymer matrices [4]. The LPE method involves exfoliating pristine powdered graphite directly in a liquid (e.g., organic solvents [5,11,12], surfactant solutions [13–15], polymers [16], ionic liquids [17]) by various sonication [5,11,18] and shear exfoliation techniques such as high-shear mixing [6,10], wet ball milling [19,20], microfluidization [21] and homogenization [22,23]. Electrochemical exfoliation, where graphene is dispersed in various electrolyte solutions could also be regarded as an LPE technique [24]. Among the different LPE techniques, high-shear exfoliation has shown potential for scalability [6,25]. In addition, it is a user-friendly, simple and cost-effective method, which can produce dispersions containing a high concentration of high-quality monolayer and few-layer graphene. These qualities enable the utilization of graphene as a low-cost electrode material in energy storage applications [26], supercapacitors [27], solar cells [28] and sensors [29].

Nanocellulose is extracted from natural biopolymer cellulose, which is a biodegradable and nontoxic material readily available from renewable sources. The abundance of cellulose sources (e.g., plant, algae, tunicate and bacteria) makes cellulose the most frequently occurring natural polymer on the Earth. Cellulose

* Corresponding author.

https://doi.org/10.1016/j.cartre.2022.100210

nanomaterials have many interesting characteristics such as low density, high surface area and good mechanical properties. One important property of nanocellulose is that it can be made colloidally stable in aqueous solutions for a wide range of salt concentrations and pH [30]. Previously, it has been shown that cellulose nanocrystals (CNC) [31] and other cellulosic nanomaterials, such as cellulose nanofibrils [32,33] and micro-nanofibrillated cellulose [33] can stabilize hydrophobic graphene in aqueous medium. In order for this stabilization to be possible, an attractive interaction must exist between nanocellulose and graphene particles. Since nanocellulose contains both hydrophilic –OH groups and hydrophobic –CH moieties, it has an amphiphilic nature. The amphiphilic nature of cellulose allows it to function as a dispersant. While the graphene-nanocellulose interaction is not fully understood, it has been suggested that there is a hydrophobic interaction between graphene and the hydrophobic part of nanocellulose [32]. Furthermore, in case of cellulose nanocrystals, the electrostatic repulsive forces between the sulfate ester groups in CNC may also play a significant role in graphene stabilization [31]. The sulfate ester groups originate from the CNC preparation process where the cellulose fibers are extracted by sulfuric acid hydrolysis.

The specific surface chemistry of nanocellulose makes it ideal for composite formation. Composites of graphene and nanocellulose have been noticed to have increased mechanical performance [32,34,35] and possess electrical conductivity [31,35] which enables applications for example in electromagnetic shielding [35]. Composites of nanocellulose and graphene-based materials have also been used as electrode materials in flexible supercapacitors [36], strain sensors [37] and humidity sensors [38,39] whereas graphene quantum dots have been used in bio-sensing applications [40]. Indeed, composite systems of graphene-based materials and cellulose nanomaterials are one of the emerging fields in the industrial transition to more sustainable materials since combining renewable polymers with graphene is beneficial for a variety of applications from environmental and economical point of view. In some cases, graphene could also replace commonly used rare and expensive heavy metals (e.g., Ga, Pt, In) in many electronic applications [41]. However, the wide-scale applications of graphene have still been hindered by low production rates and energy consuming methodologies. We also find that the use of harsh chemicals and complicated and time-consuming production methods are not in agreement with the much-needed industrial transition to more sustainable materials. Therefore, one of the main aims with this paper is to show that natural flake graphite can be quickly exfoliated to few-layer graphene in the presence of CNC with a simple and scalable method based on high-shear exfoliation resulting in dispersions with high electrical conductivity, concentration, and yield.

In addition, the biocompatibility of graphene-based materials is of increasing importance since they have recently raised interest in biological and biomedical applications [42,43]. The biocompatibility of a material is affected by its physical-chemical properties such as surface chemistry, particle size and surface charge [44]. These are not only dependent on the raw materials used but also on the production methods. In case of nanocellulose and graphene-based materials, the production methodologies vary, which leads to different surface chemistries and physical-chemical properties of the composite. This also explains why previous results regarding the biocompatibility of graphene-based materials have been inconclusive and contradictory [43].

Here, we show that a composite of graphene and CNC can be prepared by directly exfoliating graphite in a suspension of CNC using the scalable high-shear exfoliation method. This is a simple, fast and environmentally friendly method to fabricate composites since no extra chemicals or processing steps are needed. Furthermore, the composite source materials graphite [45] and cellulose are relatively low-cost and abundant making the composite even more compatible with the environmental (and ecological) requirements. In this paper, we show that using CNC as graphene stabilizer is beneficial not only for ecological and economic reasons but also for high efficiency and productivity. By optimizing the processing parameters, we were able to produce few-layer graphene dispersions with high concentration and yield. We also show that the surface charge of CNC plays a major role in stabilization as we exfoliated graphite in CNC suspensions with different amounts of negatively charged sulfate ester groups. The high graphene concentration increases the applicability of the dispersions and easily facilitates their further processing into spray-coated films. Since the electrical conductivity of the composite is of importance in electrochemical applications, we investigated the conductivity of the composite films with different concentration ratios of graphene and electrically insulating CNC. We show that the composite film can act as an excellent electron transfer layer as we investigated the electroactivity and the electrochemical stability of the composite film with cyclic voltammetry. Finally, as a proof-of-concept for using these films as electrode material in biophotovoltaic devices with photosynthetic microorganisms, we confirmed that the films are biocompatible with these cells.

2. Experimental

2.1. Materials

Natural flake graphite (d < 125 µm) from Haapamäki, Finland was used in this work. The graphite ore was enriched in an in-house process to a concentrate containing 99.3 ± 0.5% (m/m) carbon [46].

Three CNC suspensions were prepared from cellulose microcrystals (CMC) by sulfuric acid (64% v/v) hydrolysis using different acid hydrolysis times. In brief, 5 g CMC was added into sulfuric acid with a solid-liquid ratio of 1 g/10 ml. The mixtures were further hydrolyzed at 45 °C with a mechanical stirring of 150 rpm for 1.0, 1.5 and 2.0 h (hereafter denoted CNC(1.0 h), CNC(1.5 h) and CNC(2.0 h)). Then, the reaction was quenched by diluting the mixture 10-fold with deionized (DI) water and centrifuged 3 times (3200 rpm, 15 min) to remove the residual acid. After that, the solid residue was collected and dialyzed with DI water for at least 7 days until the conductivity of the DI water was lower than 1.2 µS cm^{-1} and the pH was above 6. Then, the suspension was further homogenized with a high-pressure homogenizer (ATS-AH100D, ATS Engineering Inc., China) at 1100 bar for 20 min in order to obtain the CNC suspension.

Deionized MilliQ water (resistivity 18 MΩ·cm) was used throughout this work.

2.2. Preparation of graphene-CNC dispersions

High-shear exfoliation was performed using a POLYTRON® immersion disperser (Kinematica AG, Switzerland) with a rotor-stator combination. A PT 10–35 GT drive unit was coupled with a PT-DA 20 dispersing aggregate with a rotor diameter of 15.0 mm and a rotor-stator gap of 0.30 mm. In a typical experiment, 10.0 ml of CNC suspension was first combined with a known amount of graphite (± 0.5 mg accuracy). For the preparation of highly concentrated dispersions, the mixing time (t) was 2 h, rotor speed (N) 22 000 rpm, initial graphite concentration (C(i)) 100 mg ml^{-1} (± 0.05 mg ml^{-1})) and the starting graphite-to-CNC concentration ratio was either 30:1 or 50:1. A temperature regulation system with a MGW Lauda MT bath circulator and Hetofrig (Heto, Birkerod, Danmark) water bath cooler was applied to maintain a constant temperature of 15.0 °C (± 0.4 °C). After exfoliation, the resultant graphene-CNC dispersions were left standing overnight and on the

next day, the dispersions were centrifuged for 1 h to separate and remove any unexfoliated graphite. A Hermle Z 200 laboratory centrifuge with a rotor speed of 1500 rpm corresponding to a relative centrifugal force (RCF) of 270 G was used for this purpose.

UV–vis spectra were recorded with a Shimadzu UV-2501 PC spectrophotometer to determine the concentration of the resultant dispersions. The concentration (C) was calculated according to Beer-Lambert's law, A (absorbance) = εbC (b = path length) using the absorbance value at 660 nm. The value of the extinction coefficient, ε, was previously determined to be 6600 ml mg^{-1} m^{-1} [46], which is the same value as two other independent research groups have obtained [13,47].

2.3. Characterization

2.3.1. Zeta potential

The zeta potential of CNC suspensions was analyzed with a Zetasizer Nano ZS instrument (Malvern Instruments Ltd., UK). The suspensions were diluted to a concentration of 0.1% (m/m) prior to the analysis. The samples were tested at room temperature with pH = 6–7. The reported results are an average of three measurements.

2.3.2. Atomic force microscopy

Atomic force microscopy (AFM) was used for studying the morphology of the samples prepared by immersing silanized silicon wafer plates in diluted graphene-CNC dispersions ($C \approx 0.1$ mg/ml) for 15 min followed by rinsing with water to remove any weakly attached particles. The wafers were silanized according to a previously reported procedure [40]. The positively charged silane moieties enable the attachment of the negatively charged CNC particles. AFM images were captured with an NTEGRA PRIMA (NT-MDT, Moscow, Russia) AFM instrument. 5.0 µm × 5.0 µm images (1024 × 1024 pixels) were captured in tapping mode under ambient conditions (T = 22 ± 1 °C, RH% = 58.5 ± 1.5) using silicon cantilevers with a nominal tip radius of curvature of 8 nm (Model: HQ:NSC18 / AI BS) and with a scanning rate of 0.98 – 1.30 Hz. The SPIP™ image analysis software (Image Metrology, Lyngby, Denmark) was used for image post-processing and particle size determination (Particle&Pore Analysis program).

2.3.3. Raman spectroscopy

Raman spectra were recorded with a Renishaw Ramascope imaging microscope (with the WireTM v1.3 Raman software). The spectra were recorded using an Ar-ion laser with an excitation wavelength of 514 nm and a laser power of 20 mW in the wavenumber region from 4000 to 500 cm^{-1}. The spectrometer was calibrated against a Si standard (520 cm^{-1}). The Raman spectra were collected directly from the graphite flakes without any pretreatment. For the measurement of the dispersions, ca 10 μl of liquid was deposited on a glass plate after which it was dried in an oven at 60 °C for about 15 min. At least 5 spectra of each sample were recorded.

2.3.4. Thermogravimetric analysis

Thermogravimetric analysis (TGA) of the samples was performed with an STA 449F1 *Jupiter*® (Netzsch) instrument. The analysis was conducted using nitrogen gas with a flow rate of 60 ml min^{-1} in an oxygen-free environment up to 900 °C with a heating rate of 10 K min^{-1}. The dispersions were oven-dried at 60 °C overnight prior to the analysis.

2.4. Film preparation and characterization

A standard airbrush pen was used to manually spray-coat the dispersions on thin glass substrates. Spray coating was performed on a heating plate with an electronic contact thermometer (IKA ETS-D5), which maintained a temperature between 60 and 70 °C to speed up the evaporation of water from the dispersions. The prepared films were ca 1 – 2 µm thick as measured with AFM. The film thickness was calculated based on three 100 × 100 µm AFM images (512 × 512 pixels).

2.4.1. Scanning electron microscopy

The morphologies of the graphene-CNC composite films were studied by scanning electron microscopy (SEM) using a LEO Gemini 1520 instrument with a Thermo Scientific Ultra Dry Silicon Drift Detector (SDD).

2.4.2. X-ray diffraction (XRD)

The XRD patterns for graphite, CNC and the composite films were obtained with an X-ray diffractometer (D8 DISCOVER, Bruker, Germany) using a Cu Kα radiation at 40 kV and 40 mA. Data was collected in the range of 2θ = 10–45° using a step size of 0.04° for 50 s per step. The XRD patterns were recorded from the graphite powder sample, the as-prepared composite films and CNC drop-cast on a glass substrate at a grazing incidence angle of 1°

2.4.3. Electrical conductivity

The electrical conductivity of the films was determined using the four-probe technique in a linear configuration with a tip spacing of 1.82 mm. A bias current of 1 mA was applied over the films with a Keithley 2400 SourceMeter® until a stable and reproducible voltage was obtained. The measurements were conducted under ambient conditions (T = 21.0 °C and RH% = 54.2). The film conductivities were calculated using correction factors for finite size [48].

2.4.4. Cyclic voltammetry

The graphene-CNC films on glassy carbon electrodes and on non-conductive glass substrates were electrochemically characterized with cyclic voltammetry in a three-electrode electrochemical cell using a Pt wire as a counter electrode. The area of the characterized electrodes was A = 0.50 cm^2. A single junction Ag/AgCl (3 M KCl) was used as the reference electrode. The cyclic voltammograms were recorded with an Autolab PGSTAT30 potentiostat using a Nova 2.1.3 software. The potential was cycled between –0.1 V and 0.6 V in 0.5 mM $K_3Fe(CN)_6$ (Fluka) and 0.5 mM $K_4Fe(CN)_6$ (Fluka) with 1.0 M KNO_3 (Fluka) as a supporting electrolyte using scan rates of 5, 10, 20, 50 and 100 mV s^{-1}. Five potential cycles were recorded for scan rates 20 – 100 mV s^{-1} and 2 cycles for 5 and 10 mV s^{-1} of which the last cycle is shown in the figures discussing the results of the CV measurements. Prior to all measurements, the electrolyte solution was purged with N_2 gas for at least 15 min, and during the measurements, N_2 was passed over the surface of the solution. To study the degradation in electroactivity, the composite film was cycled in the presence of the $Fe(CN)_6^{3-/4-}$ redox couple for 200 times (v = 20 mV s^{-1}) in the potential interval given above.

2.5. Cytocompatibility with photosynthetic microorganisms

A model green alga, *Chlamydomonas reinhardtii* wild-type strain CC124 (hereafter *Chlamydomonas*), was cultivated in standard Tris-acetate phosphate (TAP) medium (pH 7) [49] under continuous white light illumination of 50 μmol photons m^{-2} s^{-1} photosynthetically active radiation (PAR) at 25 °C under agitation on a rotary shaker (120 rpm) at atmospheric CO_2 levels. A model cyanobacterium, *Synechocystis* sp. PCC 6803 (hereafter *Synechocystis*), was cultured in Blue Green (BG-11) medium (pH 7.5) [50] under continuous white light illumination of 35 μmol photons m^{-2} s^{-1} PAR at 30 °C under agitation on a rotary shaker (120 rpm) at

atmospheric CO_2 levels. The cell culture growth was assessed by measuring the attenuance or optical density at 750 nm (OD_{750}) using a UV-1800 Spectrophotometer (Shimadzu). Cells were collected at OD_{750} = 1.0 and subjected to the cytocompatibility tests via measuring the photosynthetic activity (effective photosynthetic yield and photosynthetic net O_2 evolution) and cell growth when exposed to the film materials. The Chlorophyll *a* (Chl *a*) content of the *Synechocystis* cells was determined by measuring the absorbance at 665 nm from the pigment (extracted with 90% methanol). The Chl *a* content was calculated using the equation Chl *a* (μg ml^{-1}) = 12.7 × Abs at 665 nm [51]. The Chl *a* and *b* content of the *Chlamydomonas* cells were determined from the pigment extracted with 95% ethanol.

For the cytocompatibility photosynthesis measurements, 3 ml of the cell suspension (OD_{750} = 1.0) was drop-cast onto the investigated films placed in a Petri dish. Two types of composite films were investigated, and their starting graphite-to-CNC concentration ratio was either 30:1 or 50:1. In addition, a graphene film prepared by exfoliating graphite in a sodium cholate (SC) solution was investigated. A control experiment with cells drop-cast directly onto a Petri dish was also performed. The cells were incubated with the films for 80 h after which the photosynthetic activity of the cells was measured. During the incubation period, cell drying was avoided with an addition of 500–750 μl of the respective growth medium every 24 h. The effective photosynthetic yield of photosystem II, Y(II), was determined by measuring room temperature Chl fluorescence of the cells on the films using a pulse-amplitude modulation fluorimeter (PAM-2000, Walz, Germany). Prior to the measurements, the cells were dark-adapted for 10 min. Then the cells were illuminated with actinic light from above that was the same as during cultivation. Additional white light-saturating pulses (4000 μmol photons m^{-2} s^{-1}, 0.8 ms) were used to measure F′m, the maximum fluorescence under actinic light. Y(II) was calculated as (F′m-Fs)/ F′m, where Fs is the steady-state fluorescence under actinic light [52,53]. The photosynthetic net O_2 production of the cells was measured with a Clark-type electrode and chamber (Hansatech Instruments Ltd., U.K.). 1 ml of cell suspension was used for the measurements of the O_2-evolving activity without centrifugation. Then, the samples were dark-adapted for 1–2 min. The O_2 production was initiated by 1000 μmol photons m^{-2} s^{-1} white light using a Fiber-Lite DC-950 light source. The rate of O_2 production was calculated using the Hansatech software.

The cell growth when exposed to the film materials was measured on solid medium (spot test) and in liquid medium (growth curve). For the spot test, cells with a total Chl content of 5 nmol were mixed with particles extracted from graphene and graphene-CNC dispersions containing either 1 mg or 10 μg graphene in a total volume of 1 ml of the respective growth medium. The cultures were incubated for 24 h or 80 h under continuous white light illumination of 50 μmol photons m^{-2} s^{-1} at 30 °C with agitation (120 rpm) at atmospheric CO_2 levels. Cells incubated in growth medium with no dispersion particles was used as the control. After incubation, the cells were resuspended in fresh BG11 at OD_{750} = 0.5. Aliquots (10 μl) of three serial dilutions (1x, 10^{-3} and 10^{-6}) were spotted onto agar plates of the respective growth medium and incubated under 50 μmol photons m^{-2} s^{-1} at 30 °C for 7 days. Photographs were taken of the plates and growth observed to assess the cytotoxicity of the film materials. The experiment was performed in triplicate. For the growth curve, cells at a starting OD_{750} = 0.1 were mixed with the dispersion particles containing 10 μg of graphene in a total volume of 25 ml of the respective growth medium and incubated under 50 μmol photons m^{-2} s^{-1} at 30 °C with agitation (120 rpm) for 7 days. The OD_{750} was measured each day until the cultures progressed well past stationary phase (OD_{750} ~ 1.5).

3. Results and discussion

3.1. Preparation and characterization of graphene-CNC dispersions

In order to optimize the exfoliation process in CNC to produce as highly concentrated dispersions as possible, graphite exfoliation was carried out using different rotor speed, *N*, initial graphite concentration, *C*(i), time, *t* and CNC concentration. We found that the graphene concentration increases as a function of *N* (up to 24 000 rpm), *C*(i), *t* (up to *t* = 120 min) and CNC concentration (Fig. 1). The decline in graphene concentrations after *N* = 24 000 rpm and *t* = 120 min might be due to degradation of CNC caused by high-energy exfoliation conditions (Fig. 1A and C). Previously, Malho et al. observed that sonication energies higher than 6 kJ led to lower tensile strength and modulus values of cellulose nanofibrils (CNF) [32]. As can be seen in Fig. 1D, the graphene concentration increases with increasing CNC concentration and decreasing graphite-to-CNC concentration ratio (hereafter, graphite-to-CNC ratio) *t* for both initial graphite concentrations (*C*(i) = 50 and 75 mg ml^{-1}, *t*=15 min), as expected. We used different *C*(i) in order to investigate if the stabilization is more dependent on solely the CNC concentration or on the ratio between graphite and CNC concentrations. Although the increase in the graphene concentration levels out towards higher CNC concentrations, there seems to be no specific CNC concentration or concentration ratio where a maximum graphene concentration is reached in contrary to our previous results using sodium cholate (SC) as dispersant [46]. With SC-stabilized graphene, there was a clear maximum SC concentration after which the graphene concentration started to decline. This was explained by the micelle depletion mechanism of surfactants, which does not apply to CNC since it does not have the ability to form micelles. Thus, there are differences in the stabilization mechanisms. Nonetheless, the ability of CNC to stabilize graphene is linked to its amphiphilic nature.

In order to gain more understanding about the stabilization mechanism and interaction between graphene and CNC, graphite was exfoliated in CNC suspensions, which were prepared with different acid hydrolysis times of 1.0 h, 1.5 h and 2.0 h. As expected, the measured zeta potential value of the CNC suspensions correlates with the duration of sulfuric acid hydrolysis as can be seen in the inset of Fig. 2. During sulfuric acid hydrolysis, sulfuric acid reacts with the surface hydroxyl groups of CNC creating anionic sulfate ester groups (-OSO_3^-), which induce a negative surface charge on the CNC rods [54–57]. The duration of acid hydrolysis affects the amount of the negatively charged sulfate ester groups and a more negative surface charge is exhibited as lower zeta potential values [55,57–59]. Indeed, the zeta potential was almost twice as low for the CNC(2.0 h) sample than for the CNC(1.0 h) sample. However, the difference in zeta potential after 1.5 h and 2.0 h acid hydrolysis was relatively small. Under the reaction conditions used for the sulfuric acid hydrolysis, the oxidation reaction to the hydroxyls on cellulose surface might have reached near a saturation. As can be seen in Fig. 2, the concentration of the exfoliated sheets was almost proportional to the value of zeta potential as the lowest zeta potential value gives the highest graphene concentration. The graphene concentration was ca 32% higher after *t* = 2 h using CNC(2.0 h) compared to CNC(1.0 h). This indicates that the negative surface charge of CNC plays a significant role in the stabilization of graphene.

Since CNC is electrically insulating, a lower dispersant concentration would increase the conductivity of the films even if a higher graphene concentration could be achieved by increasing the CNC concentration. Therefore, there is a balance to be found between maximizing the graphene concentration with the help of CNC and the electrical conductivity of the composite. In order to do this, we exfoliated graphite by using CNC(1.0 h) for 2 h

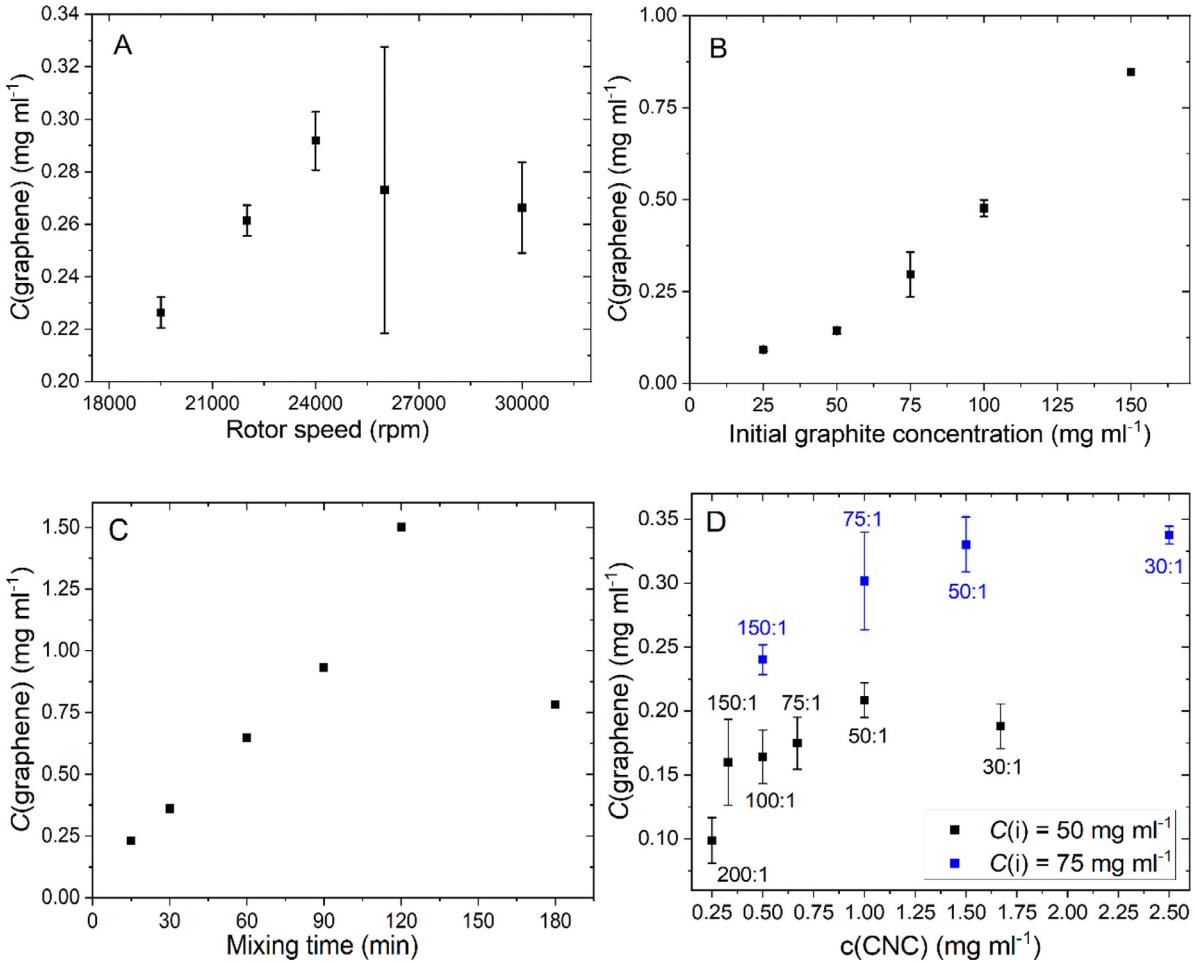

Fig. 1. A and B. Graphene concentration as a function of rotor speed with $C(i) = 50$ mg ml^{-1} (A) and as a function of initial graphite concentration with $N = 22\,000$ rpm (B) using $t = 15$ min, 50:1 graphite-to-CNC ratio and CNC(2.0 h). The results are an average of three experiments, except with $C(i) = 150$ mg ml^{-1} where $n = 1$. Figure 1 C and D. Graphene concentration as a function of mixing time with $C(i) = 50$ mg ml^{-1} and 50:1 graphite-to-CNC ratio using CNC(2.0 h) (C) and as a function of CNC concentration with $C(i) = 50$ mg ml^{-1} (black squares) and 75 mg ml^{-1} (blue squares) using CNC(1.0 h) and $t = 15$ min (D) with $N = 22\,000$ rpm. Graphite-to-CNC ratio is shown for each data point. The results are an average of three measurements (D).

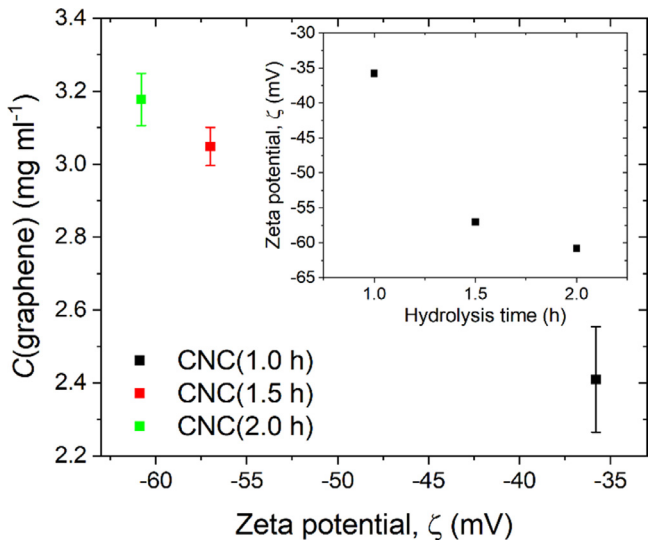

Fig. 2. Graphene concentration as a function of zeta potential using $N = 22\,000$ rpm, $C(i) = 100$ mg ml^{-1}, $t = 2$ h and 50:1 graphite-to-CNC ratio. The results are an average of three experiments. The value in parenthesis is the duration of sulfuric acid hydrolysis of CNC. The zeta potential as a function of sulfuric acid hydrolysis time is shown in the inset.

($C(i) = 100$ mg ml^{-1}) using four different graphite-to-CNC ratios from 100:1 to 30:1 (the composite films prepared from these dispersions are discussed in Section 3.2). As can be seen in Fig. 3 (and Table 1, Section 3.2), the graphene concentrations are 4.0 and 2.4 mg ml^{-1} using 30:1 and 50:1 graphite-to-CNC ratios, respectively. With higher graphite-to-CNC ratios (75:1 and 100:1), the resulting graphene concentrations are under 0.05 mg ml^{-1}, which is lower than after $t = 15$ min using the same concentration ratios (Fig. 1D) and no films could be prepared from these dispersions. Furthermore, the dispersions were not stable, and they flocculated within a few days after preparation. It seems that with these concentration ratios, there is not enough CNC to stabilize graphene and that there is a threshold ratio between 75:1 and 50:1 where the stabilization starts to be effective when a longer mixing time is used. Nevertheless, the concentrations (and yields) reported here are high, up to 4.0 mg ml^{-1} using 30:1 graphite-to-CNC ratio. In our previous work using SC surfactant solution as dispersing medium, we reported 3.0 mg ml^{-1} using the same method as reported here ($t = 2$ h and $C(i) = 100$ mg ml^{-1}). The concentration that we reported was the highest achieved using environmentally friendly aqueous based dispersing agents with the shear mixing method [46]. This result show that CNC is a very good graphene stabilizer. In addition, the concentrations achieved in this study are higher than previously reported when nanocellulose was

Table 1
The average graphene concentrations and film conductivities with t = 2 h, C(i) = 100 mg ml^{-1} and N = 22 000 rpm using CNC(1.0 h). The concentration is an average of three exfoliations and the dispersions were combined after exfoliation. The film thickness and the conductivity results are an average of three films.

Starting graphite-to-CNC conc. ratio	Starting CNC conc. (mg ml^{-1})	Graphene conc. (mg ml^{-1})	Graphene yield (%)	Graphene amount from TGA (% m/m)	Average film thickness (nm)	Conductivity (S m^{-1})
50:1	2.0	2.4 ± 0.1	2.4	Ca 74	1010 ± 40	280 ± 30
30:1	3.3	4.0 ± 0.4	4.0	Ca 60	1600 ± 300	108 ± 33

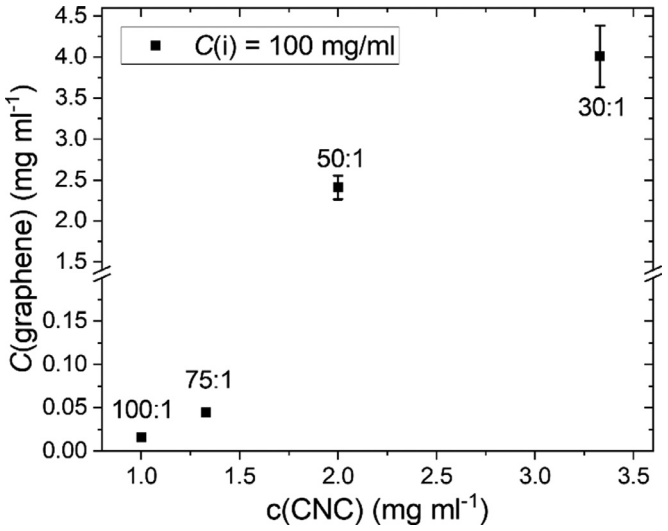

Fig. 3. Graphene concentration as a function of CNC concentration with C(i) = 100 mg ml^{-1}, N = 22 000 rpm and t = 2 h using CNC(1.0 h). Graphite-to-CNC ratio is shown for each data point. The results are an average of three measurements, except with 75:1 and 100:1 where n = 1 and 2, respectively.

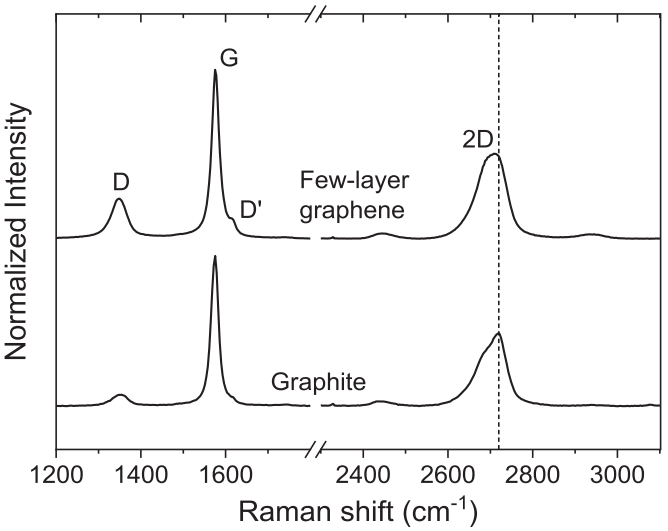

Fig. 4. Raman spectra of graphite (d < 125 µm) and few-layer graphene exfoliated from it in a suspension of CNCs (50:1 graphite-to-CNC ratio) with t = 2 h. The results are an average of five spectra normalized to the G band intensity.

used as a dispersing medium [31,39] showing the effectiveness of the applied shear exfoliation method.

To find evidence of exfoliation, we analyzed a highly concentrated graphene dispersion (50:1 graphite-to-CNC ratio, t = 2 h) with Raman spectroscopy and AFM. Fig. 4 shows the averaged Raman spectra of the starting graphite and the graphene-CNC composite. The Raman spectrum of pristine graphite shows prominent G (1575 cm^{-1}) and 2D (2721 cm^{-1}) bands and a less intensive defect induced D band (1355 cm^{-1}), all characteristic for graphitic material [54]. After exfoliation, the spectrum resembles typical few-layer graphene as the 2D band has downshifted to a lower wavenumber and it has become more symmetric compared to the starting material indicating that the number of layers has decreased [60–62]. The 2D band of graphene with five or more layers is very similar to that of graphite [61–63]. The 2D bands of CNC-stabilized graphene and graphite have clearly different shapes indicating that after exfoliation, the dispersion mostly contains graphene with less than five layers.

The D/G intensity ratio had increased after exfoliation. The defects associated with the D band can be edges including grain boundaries and flake edges or topological (basal plane) defects in the sheet [64]. With liquid-phase exfoliated graphene, the increased D band intensity has generally been attributed to the formation of new edges as the flake size is decreased during exfoliation [10,25]. The decrease in the lateral particle size was also confirmed by AFM results (see below). In addition, the D/D' intensity ratio (4.4 ± 0.3) also indicates that the defects are of edge type since boundary and edge defects give rise to D/D' ≈ 3.5 - 4.5 [6,65]. Since the D/D' intensity ratio is within the margins for boundary type defects, it can be stated that no defects other than new edges were probably formed during the CNC-stabilized shear exfoliation process.

Figs. 5 and 6 show AFM images of graphene-CNC dispersions which were prepared with 30:1 and 50:1 graphite-to-CNC ratios, respectively. The AFM samples were prepared by dipping a silanized Si wafer into the diluted graphene-CNC dispersion as described in the experimental section. In both figures, thin flake-like particles with sharp edges can be observed, representing the exfoliated graphene sheets. These exfoliated sheets have varying lateral dimensions ranging from tens of nanometers to ca 1 µm. We performed a detailed statistical analysis on the 50:1 sample using three AFM images, which showed that the majority of the exfoliated sheets were relatively small, under 100 nm in length (Fig. 7A). The thickness of the exfoliated sheets was also estimated with AFM, bearing in mind that the measured height of the particles is larger than the theoretical thickness of graphene layers since the dispersant adsorbed on graphene also contributes to the measured height [1,6,46]. The statistical analysis showed that the apparent thickness of ca 47% of the sheets was under 3 nm (Fig. 7B), which corresponds to maximum 5 layers of graphene [1]. This result is in agreement with Raman analysis and confirms the presence of few-layer graphene. In addition to the exfoliated sheets, some rod-like particles were also present in the AFM images (indicated with black arrows in Fig. 5A), which could be identified to represent CNC since they resemble the CNC nanorods in the reference pure CNC sample being shown in the inset of Fig. 5A. These 20–30 nm wide nanorods have varying lengths from ca 100 to 600 nm and heights from ca 1 to 5 nm. Some spherical particles with ca 20–30 nm diameter can also be identified. Some of these CNC particles are dispersed among the graphene sheets and some are in contact with the exfoliated graphene sheets as can be seen in both topographical (Figs. 5 and 6A) and phase contrast images (Figs. 5 and 6B). The rod-like CNC particles have a slightly darker phase contrast compared with the graphene particles, which arises from a material contrast between CNC and graphene based on their characteristic viscoelastic properties [66].

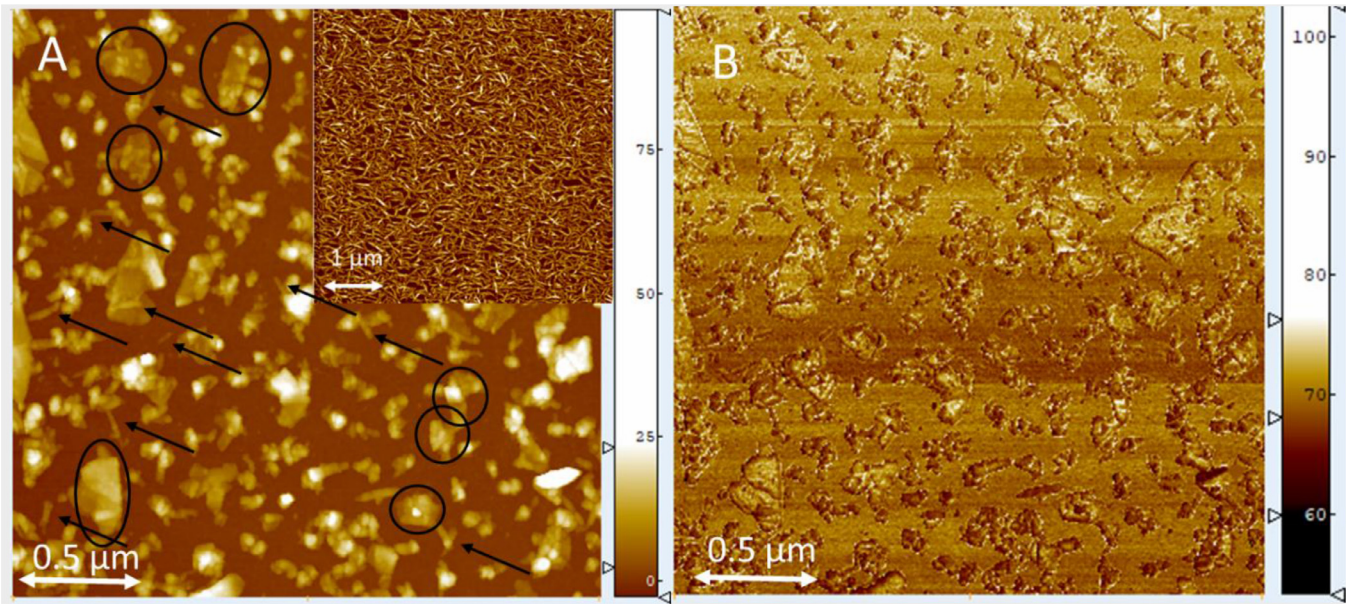

Fig. 5. A 2.5 x 2.5 µm top-view topographical AFM image (A) and its phase contrast image (B) of few-layer graphene exfoliated (t = 2 h) in a CNC suspension (30:1 graphite-to-CNC ratio) and deposited on a silanized Si wafer. A 5.0 x 5.0 µm top-view topographical AFM image of pure CNC(1.0 h) used in the exfoliation is shown in the inset. Some typical exfoliated sheets are circled and typical CNC nanorods are indicated with black arrows.

Fig. 6C represents an enlargement of a 0.8 x 1.0 µm area of the phase image where, based on the material-specific phase contrast, a CNC nanorod can be resolved on the surface of the few-layer graphene sheet. The line profile graph (Fig. 6D) along the line indicated in Fig. 6C confirms that there is a difference in phase shift of approximately 2.0° arising from the compositional contrast between CNC and graphene. Besides compositional (material) contrast there is a topographical contrast arising from increased tip-sample contact area at structural grain boundaries, appearing as edge effects in the phase contrast image, i.e. a sharp dip and peak on either side of the rod in the line profile [66]. These artifacts can be omitted, leaving the material contrast between the CNC rod and the underlying graphene flake. The height of 5 nm and width of ca 30 nm of the rod particle from the corresponding topograph (Fig. 6A) confirms that the particle represents a CNC particle (c.f. the inset of Fig. 5A). The CNC nanorods are more abundant in the 30:1 sample (Fig. 5) than in the 50:1 sample (Fig. 6) showing that the smaller graphite-to-CNC ratio (30:1 vs. 50:1) also yields a larger amount of CNC in the dispersion. This is in agreement with the TGA results (see Table 1).

3.2. Characterization of the graphene-CNC composite films

Finally, we prepared composite films from the highly concentrated few-layer graphene dispersions (C = 2.4 and 4.0 mg ml^{-1}) by spray-coating on thin glass substrates. The electrical conductivity of the films prepared from dispersions with 50:1 and 30:1 starting graphite-to-CNC ratios (hereafter 50:1 and 30:1 films) were 280 S m^{-1} and 108 S m^{-1}, respectively (Table 1). The film with the higher conductivity contained more graphene and consequently less CNC compared to the film with the lower electrical conductivity. The graphene contents of the 50:1 and 30:1 films were 74 and 60% (m/m) (estimated with TGA), respectively, which gave 2.6 times higher conductivity to the 50:1 film. That is, the starting graphite-to-CNC ratio and the consequent CNC amount in the films have a significant effect on the conductivity. Due to the insulating nature of nanocellulose, it has been challenging to prepare composites with a high conductivity. The previously reported values for composites of nanocellulose and graphene-based materials vary from non-conductive [32] to ca 5000 S/m which was achieved by layer-by-layer assembly of rGO and CNC [67]. Typically, values under 100 S/m have been reported [30,33,39,68–70]. To this end, the electrical conductivities of 108 and 280 S m^{-1} are among the highest reported.

The surface morphology of the films also affects their conductivity. The SEM images of the film surfaces (Fig. 8) show that it is composed of graphene flakes with a varying length from <100 nm to several hundreds of nanometers (in agreement with the AFM results, Fig. 6 and 7) with some visible junctions between the flakes. The porosity (the size and number of inter-flake junctions) of a graphene nanosheet network has been linked with its conductivity [71,72] since the inter-flake junctions decrease the electron mobility in the film and thereby increase the resistance in the system. Based on the SEM images, no clear differences in the morphologies of 50:1 and 30:1 films can be distinguished indicating that the CNC amount in the film is the main cause for the different film conductivities.

Fig. 9 shows the XRD patterns of the graphite starting material, pure CNC and 30:1 and 50:1 composite films. The neat CNC drop-cast on a glass substrate shows peaks at 2 θ = 14.9°, 16.4°, 22.6° and 34.4° corresponding to the crystalline planes of (1–10), (110), (200) and (004), respectively, which are characteristic of cellulose I allomorph structure [73–75]. The crystallinity of the as-prepared CNC is 78.0% as calculated with the Segal's method [76]. Graphite and the composite films show a prominent peak at 2 θ = 26.5° which corresponds to the (002) crystalline plane of graphite and a layer-to-layer d-spacing of 0.3358 nm. However, the (002) peaks of the composite films are broader and more asymmetric towards lower angles compared to graphite. This indicates that graphite has successfully been exfoliated to few-layer graphene. In addition, the characteristic CNC peaks are also present in the XRD pattern of the composite films. The (200) diffraction peak, which is related to the thickness of the molecular sheets in the stacking direction of the a-axis of the cellulose unit cell [77] is the clearest cellulose peak in the composite films. It is also more prominent for the 30:1 composite film, which contains more CNC than the 50:1 composite film. The other CNC peaks in the composite films can be discerned at higher magnifications.

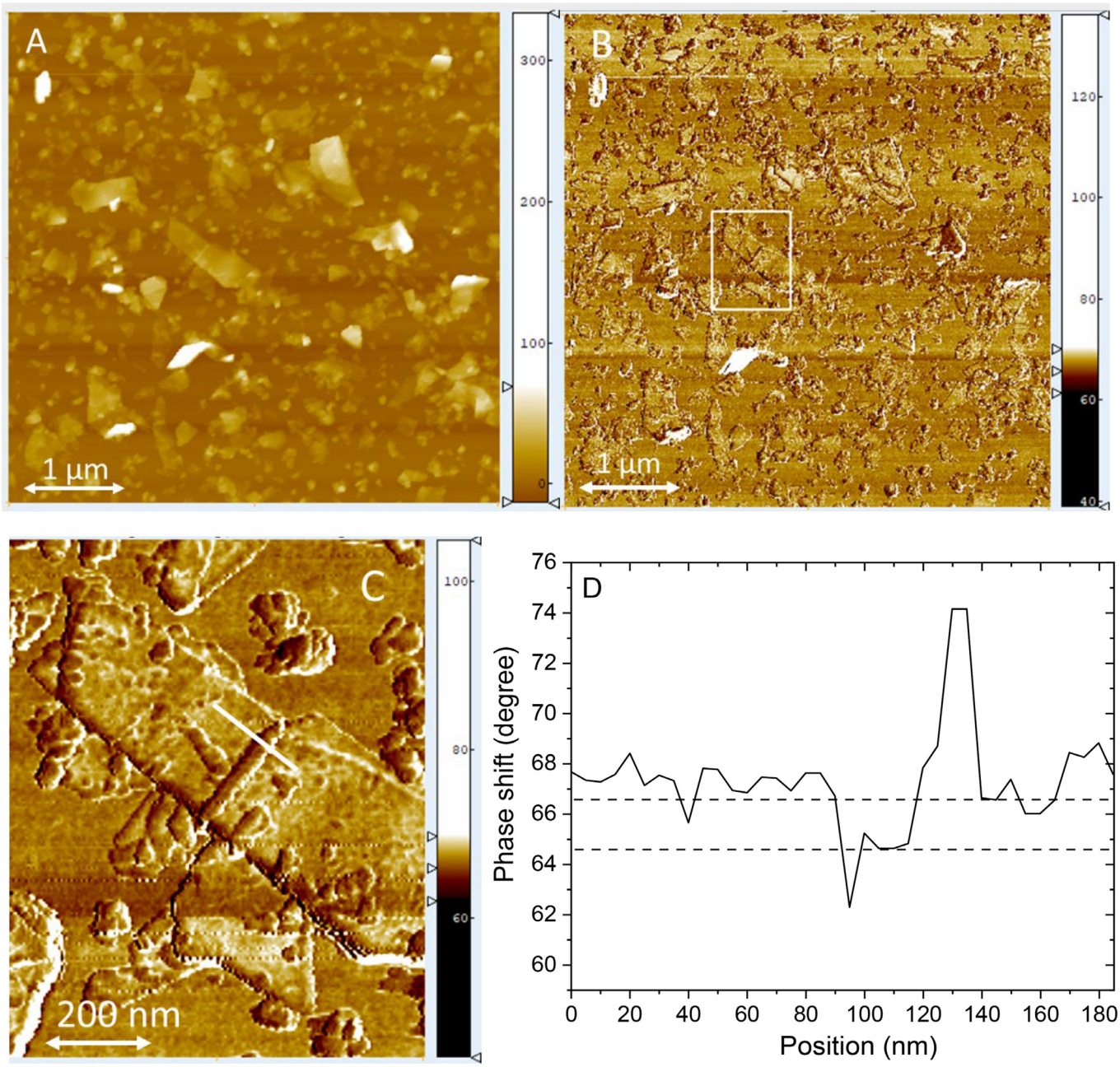

Fig. 6. A 5.0 x 5.0 µm top-view topographical AFM image (A), a phase contrast image of the same area (B) and an enlargement of 0.8 x 1.0 µm area (C) of the phase contrast image of few-layer graphene exfoliated (t = 2 h) in a CNC suspension (50:1 graphite-to-CNC ratio) and then deposited on a silanized Si wafer. Also included is a line profile (D) along the line indicated in the phase contrast image (C).

The electrochemical properties of the 50:1 graphene-CNC films on a glassy carbon (GC) electrode and on a non-conductive glass substrate were characterized by cyclic voltammetry (CV). Fig. 10A shows the cyclic voltammograms of the 50:1 graphene-CNC film on a commercial GC electrode in comparison to a bare GC electrode in an aqueous solution consisting of 0.5 mM $K_3Fe(CN)_6$ and 0.5 mM $K_4Fe(CN)_6$ with 1.0 M KNO_3 as the background electrolyte. The same GC electrode was used for both measurements. Well-defined reduction and oxidation peaks of the $Fe(CN)_6^{3-/4-}$ redox couple are observed for both electrodes whereas the redox peaks are absent in the pure KNO_3 solution where only the background current can be seen (i.e., the capacitive charging current due to the double layer formation). The relatively high capacitive current of the graphene-CNC film indicates that the surface and most likely also the bulk of the composite film are porous resulting in a much higher active surface area compared to the flat and smooth GC surface. The redox response of the graphene-CNC film indicates also that the electrically insulating CNC does not hinder the electron transfer through the composite film and that the graphene-CNC network offers continuous electron transfer pathways, which is in good accordance with the electrical conductivity measurements showing that the composite films are electrically conducting. In addition, the redox potentials of the graphene-CNC film on non-conductive glass (Figs. 10B and 11) are practically the same as for the GC electrode indicating that the GC substrate does not contribute to the observed current of the graphene-CNC film. The

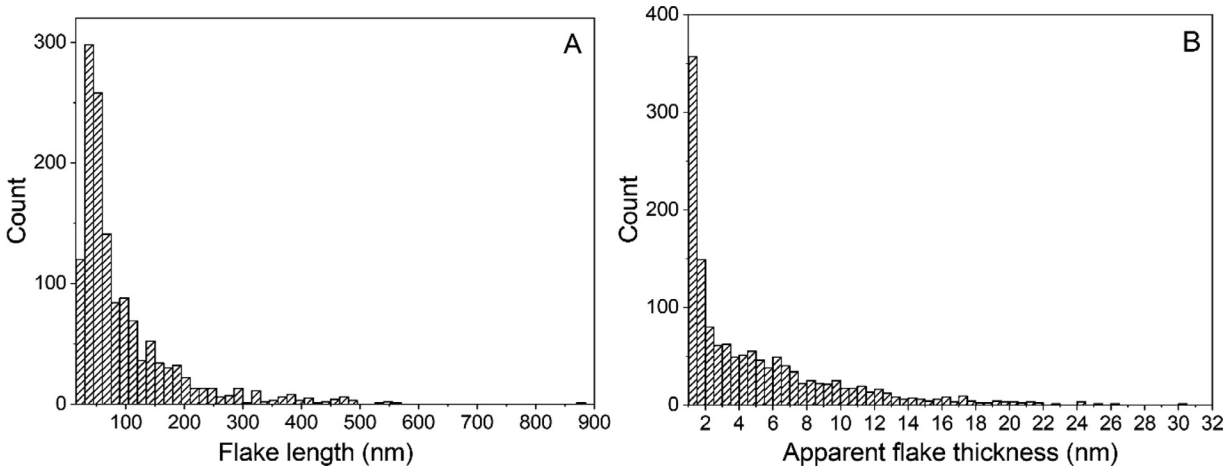

Fig. 7. A statistic histogram representing the flake length (A) and apparent thickness (B) distribution of the exfoliated sheets dispersed in CNC based on the combined data from three AFM images of the same sample.

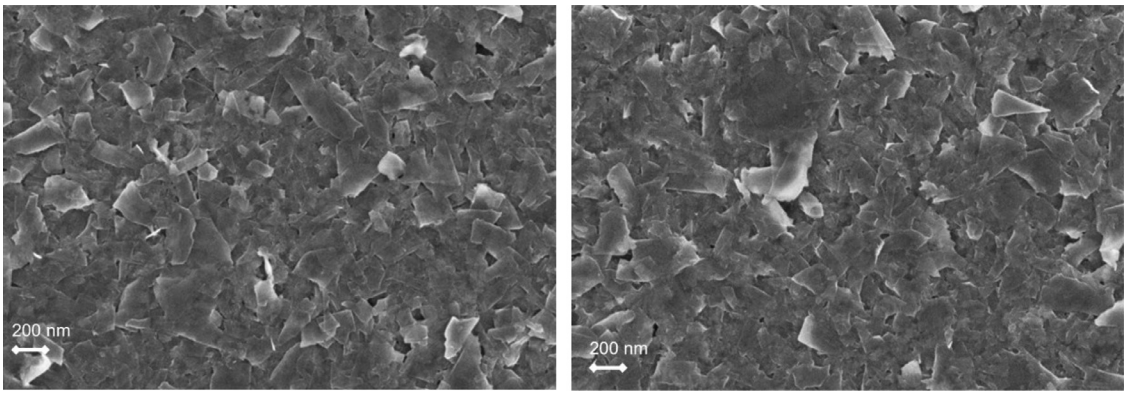

Fig. 8. Top-view high magnification (25000x) SEM images of spray-coated 30:1 (on the left) and 50:1 (on the right) graphene-CNC composite films.

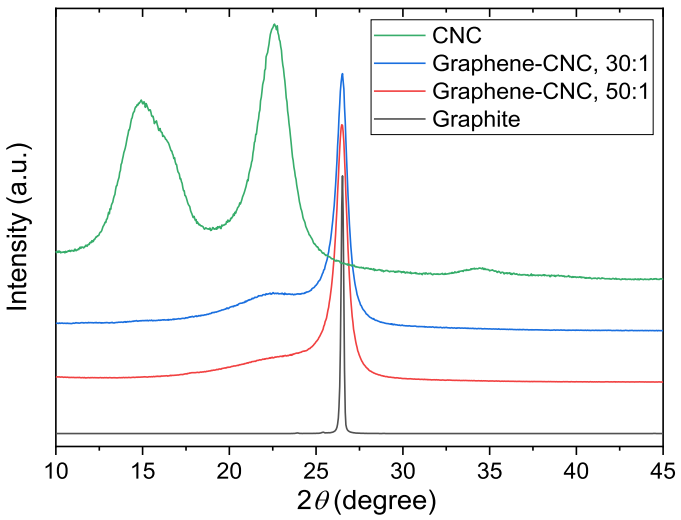

Fig. 9. Normalized XRD patterns of graphite (d < 125 µm) and CNC starting materials and graphene-CNC composite films with 50:1 and 30:1 graphite-to-CNC ratios.

differences in the current densities in Fig. 10A (GC substrate) and Fig. 11A (non-conductive glass substrate) are due to differences in the graphene-CNC film thickness.

The degradation of the electroactivity of the composite film on the non-conductive glass substrate in contact with water was studied by continuous potential cycling for 4 h. As can be seen in Fig. 10B, the redox response is unchanged over the entire measurement indicating a high stability of the electrochemical response. It can be speculated that the reason for the very good water-stability of the composite film is the relatively low amount of CNC in the film matrix acting as a binder keeping the more hydrophobic graphene sheets together. The hydrophobicity of graphene prevents the solubilization of the composite films in the aqueous solution during the time scale of the stability measurement (4 h).

Table 2
The anodic ($E_{p,a}$) and cathodic ($E_{p,c}$) peak potentials, and the peak separation (ΔE_p) for the graphene-CNC film (50:1) on GC electrode and for bare GC electrode measured in 1.0 mM $Fe(CN)_6^{3-/4-}$ (see Fig. 8A); v = 50 mV s^{-1}.

Electrode	$E_{p,a}$ (V)	$E_{p,c}$ (V)	ΔE_p (V)
Graphene-CNC	0.305	0.213	0.092
GC	0.300	0.222	0.078

Table 2 shows the anodic ($E_{p,a}$) and cathodic ($E_{p,c}$) redox peak potentials and peak separation (ΔE_p) of the 50:1 film on GC electrode and bare GC electrode measured at 50 mV s^{-1} in the $Fe(CN)_6^{3-/4-}$ redox solution. The peak separation is only somewhat larger for the 50:1 film (0.092 V) than for the GC electrode (0.078 V) indicating that the redox reaction has almost the same reversibility on the bare GC electrode surface and on the graphene-CNC film. Additionally, the CVs in Fig. 11 show that the reversibility of the $Fe(CN)_6^{3-/4-}$ redox couple is very good even at higher scan rates for the 50:1 film electrode (on non-conductive glass substrate). The peak separation increases from 65 mV, which is very

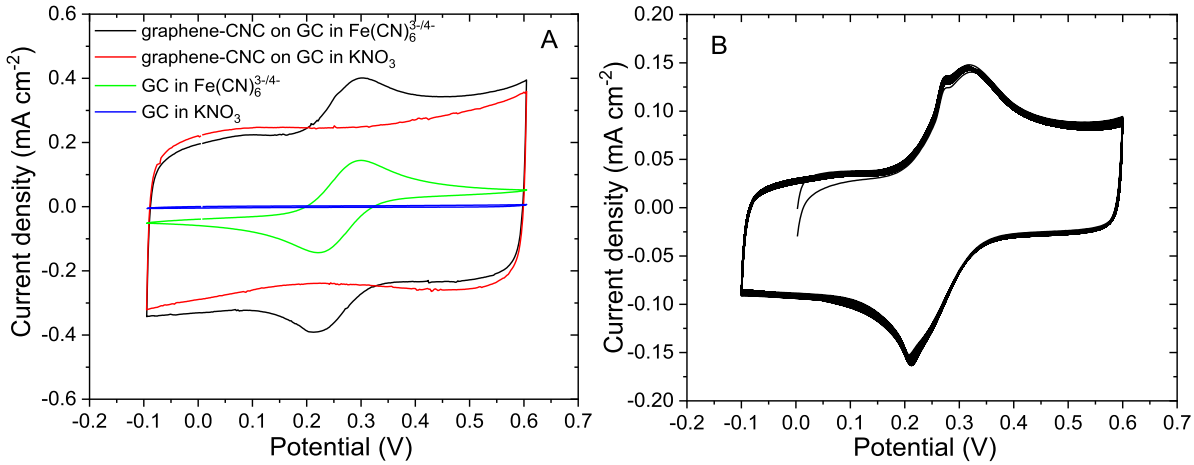

Fig. 10. Cyclic voltammograms of the graphene-CNC film (50:1) on GC electrode and of bare GC electrode in 0.5 mM $K_3Fe(CN)_6$ and 0.5 mM $K_4Fe(CN)_6$ with 1.0 M KNO_3 as the background electrolyte, and in pure 1.0 M KNO_3; vF = 50 mV s^{-1} (A). Cyclic voltammograms of the 50:1 film on non-conductive glass substrate in 0.5 mM $K_3Fe(CN)_6$, 0.5 mM $K_4Fe(CN)_6$ and 1.0 M KNO_3; 200 potential cycles, t = 4 h, v = 20 mV s^{-1} (B).

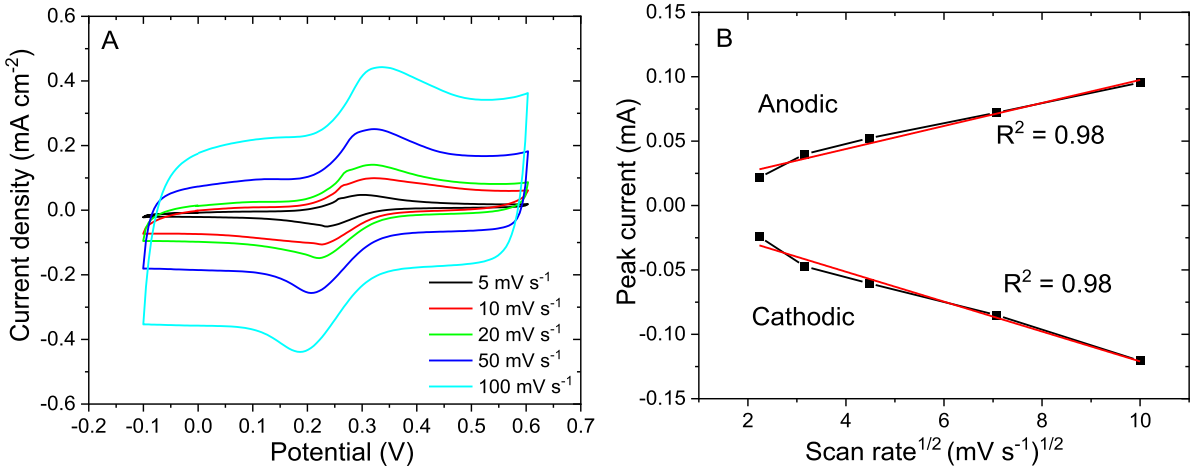

Fig. 11. Cyclic voltammograms of the graphene-CNC film (50:1) in 0.5 mM $Fe(CN)_6^{3-}$, 0.5 mM $Fe(CN)_6^{4-}$ and 1.0 M KNO_3 measured with different scan rates from 5 to 100 mV s^{-1} (A) and the anodic and the cathodic peak currents as a function of the square roots of the scan rates (B).

close to the theoretically expected peak separation of 59.2 mV for a one electron process at 25 °C, to only 116 mV when the scan rate is increased from 5 to 50 mV s^{-1}, showing that the electron transfer is efficient in the bulk and on the surface of the composite film. In addition, the linear dependence of the anodic and cathodic peak currents vs. the square root of the scan rate reveals that the redox reaction is diffusion controlled (Fig. 11B), although the scan rate of 5 mV s^{-1} deviates slightly from the linearity.

3.3. Biocompatibility of the graphene-CNC composite films

The biocompatibility of the 50:1 and 30:1 graphene-CNC composite films with prokaryotic (*Synechocystis*) and eukaryotic (*Chlamydomonas*) photosynthetic microorganisms was evaluated. In addition, a few-layer graphene film prepared by exfoliating graphite in SC solution with no CNC was investigated. The biocompatibility was evaluated on two fronts: photosynthetic activity and cell growth. Schematic presentations of the studied cells and biocompatibility measurements are shown in Fig. 12.

To measure the photosynthetic activity, a thin layer of the cells was applied on the films allowing a direct contact of the material with the cells. The photosynthetic performance of the cells interacting with the films was evaluated as the change in the effective yield of photosystem II, Y(II) and relative photosynthetic net O_2 evolution values (for more details, see the experimental section). These values are common indicators of photosynthetic activity and are sensitive to environmental stress [78]. Both *Chlamydomonas* and *Synechocystis* cell layers on the films exhibited similar Y(II) parameters (Fig. 12B) and photosynthetic O_2 evolving activity (Fig. 12C) as control cells that were not exposed to the films and no significant difference between the film types was observed. Therefore, the films maintain the photosynthetic activity of the microbes, making them suitable as bio-anodes for biophotovoltaic devices where current is harvested from photosynthetic electron transfer chain [79]. To measure the effect on cell growth, the cells were exposed to graphene-CNC and few-layer graphene dispersion particles in their liquid growth medium and their subsequent growth on either solid or liquid medium was measured. Both *Chlamydomonas* and *Synechocystis* cells exhibited similar growth on solid medium after exposure to dispersion particles for up to 80 h compared to control cells that were not exposed (Fig. 12D). Similarly, both *Chlamydomonas* and *Synechocystis* cultures grew in liquid medium containing dispersion particles (Fig. 12D). The results obtained here indicate that the few-layer graphene and graphene-CNC composite films prepared by exfoli-

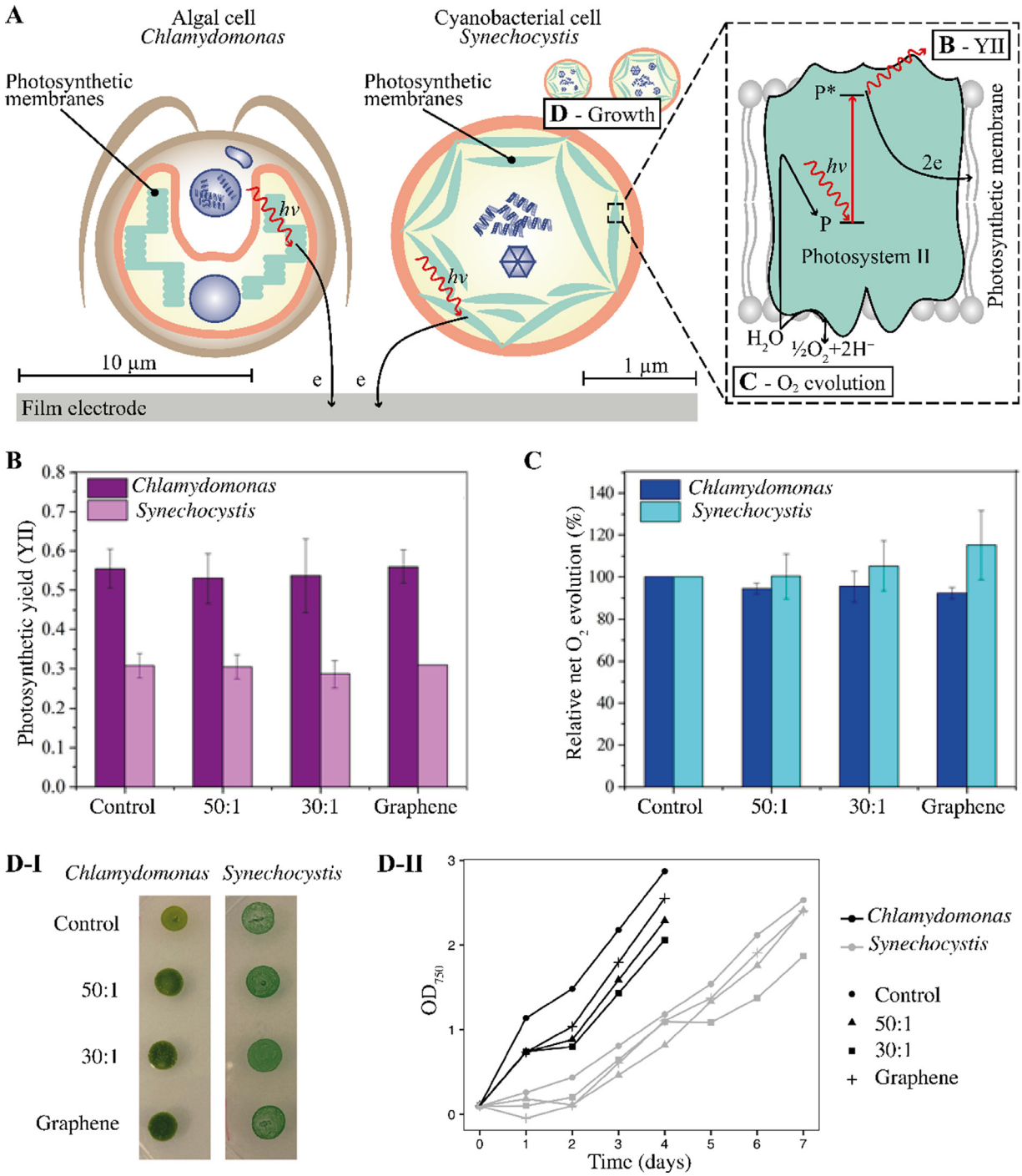

Fig. 12. (A) Schematic representations of cells of the model alga *Chlamydomonas reinhardtii* and model cyanobacterium *Synechocystis* sp. PCC 6803. The inset represents a photosystem II (PSII) complex (a photocatalyst for water oxidation and generation of electrons) embedded in the photosynthetic membrane. The biological components assayed for biocompatibility are labelled B-D. (B) The effective yield of photosystem II, Y(II) and (C) photosynthetic net O_2 evolution activity of cells on the 50:1 and 30:1 graphene-CNC films and graphene exfoliated in SC (graphene) after 80 h of incubation. The control cells were incubated on a petri dish with no film exposure. Error bars correspond to the means of standard error values derived from two independent biological replicates. Each biological replicate represents 1–3 independent measurements. (D-I) A photograph of cells after 7 days of incubation on solid medium (agar plate) after 80 h exposure to graphene and graphene-CNC dispersion particles. The photograph is representative of three biological replicates. (D-II) The optical density (OD_{750}) of cells grown in liquid medium mixed with dispersion particles measured each day up to 7 days.

ating graphite in liquid phase exhibit good biocompatibility and no cytotoxicity toward model eukaryotic and prokaryotic photosynthetic microorganisms upon prolonged incubation (80 h), making them useful for long-term bioelectrochemical applications where photosynthetic microorganisms are employed as living biocatalysts [79,80].

4. Conclusions

A fast, facile, low-cost and environmentally benign one-step process for the preparation of graphene-CNC composite dispersions was achieved by exfoliating natural flake graphite directly in CNC suspensions. Graphite was exfoliated in CNC suspensions

with different amounts of sulfate ester groups, and we have shown that the electrostatic repulsion provided by these negatively charged surface groups had a significant effect on the concentration of graphene dispersions. With the optimized shear exfoliation method, highly concentrated defect-free few-layer graphene dispersions were prepared only after 2 h exfoliation. The graphene concentration increased with increasing CNC concentration, and we were able to prepare dispersions with few-layer graphene as high as 4.0 mg/ml showing that CNC is an excellent graphene stabilizer. The higher initial CNC concentration had a significant effect on the conductivity of the spray-coated graphene-CNC composite films as the conductivity decreased from 280 S m^{-1} (50:1) to 108 S m^{-1} (30:1). Furthermore, the 50:1 film acted as an efficient electron transfer layer as the $Fe(CN)_6^{3-/4-}$ redox reaction occurred reversibly on its surface. The biocompatibility of the graphene-CNC films towards photosynthetic microorganisms is promising especially for electrical energy generation in photovoltaic applications, such as biophotovoltaic devices. In combination with good water-stability, the composite films may be useful also in small scale energy storage applications, like flexible batteries and supercapacitors.

Declaration of Competing Interests

The authors declare that they have no known competing financial interests or personal relationships that could have appeared to influence the work reported in this paper.

CRediT authorship contribution statement

Sara Lund: Conceptualization, Methodology, Investigation, Formal analysis, Visualization, Writing – original draft, Writing – review & editing, Supervision, Funding acquisition. **Elisabeth Björnvik:** Investigation, Validation. **Qingbo Wang:** Investigation, Writing – original draft. **Xiaoju Wang:** Resources, Supervision, Writing – review & editing. **Sindhujaa Vajravel:** Investigation, Formal analysis, Visualization, Writing – original draft. **Laura T. Wey:** Investigation, Formal analysis, Visualization, Writing – original draft, Writing – review & editing. **Yagut Allahverdiyeva:** Resources, Writing – review & editing, Supervision, Funding acquisition. **Jussi Kauppila:** Conceptualization, Writing – review & editing, Supervision. **Jan-Henrik Smått:** Resources, Writing – review & editing, Supervision, Funding acquisition. **Jouko Peltonen:** Resources, Writing – review & editing, Supervision, Funding acquisition. **Rose-Marie Latonen:** Resources, Writing – review & editing, Supervision, Funding acquisition. **Tom Lindfors:** Conceptualization, Resources, Writing – review & editing, Supervision, Funding acquisition.

Acknowledgements

This work was funded by the Academy of Finland (grant number 292472), Finnish Foundation for Technology Promotion, K.H. Renlund foundation, Novo Nordisk Foundation project “PhotoCat” (no. NNF20OC0064371 to Y.A) and Kone foundation (project number 201608799). The authors greatly acknowledge Lic.*Sc*. Jenny Palosaari from Department of Geology and Mineralogy, Åbo Akademi University (ÅAU), M.*Sc*. Rasmus Blomquist and M.*Sc*. Sauli Raunio from Grafintec Oy (Beowulf Mining) for providing the graphite-bearing rock samples from Haapamäki, Finland. Dr. Sergey Kosourov is acknowledged for his advice regarding the biocompatibility of photosynthetic microbes. SmartBio Biocity Turku Research program is acknowledged for stimulating multidisciplinary collaboration.

References

[1] K.S. Novoselov, A.K. Geim, S.V. Morozov, D. Jiang, Y. Zhang, S.V. Dubonos, I.V. Grigorieva, A.A. Firsov, Electric field effect in atomically thin carbon films, Science 306 (2004) 666–669, doi:10.1126/science.1102896.
[2] B. Hu, H. Ago, Y. Ito, K. Kawahara, M. Tsuji, E. Magome, K. Sumitani, N. Mizuta, K. Ikeda, S. Mizuno, Epitaxial growth of large-area single-layer graphene over Cu(111)/sapphire by atmospheric pressure CVD, Carbon N Y 50 (2012) 57–65, doi:10.1016/j.carbon.2011.08.002.
[3] H. Zhou, W.J. Yu, L. Liu, R. Cheng, Y. Chen, X. Huang, Y. Liu, Y. Wang, Y. Huang, X. Duan, Chemical vapour deposition growth of large single crystals of monolayer and bilayer graphene, Nat. Commun. 4 (2013) 2096, doi:10.1038/ncomms3096.
[4] V. Nicolosi, M. Chhowalla, M.G. Kanatzidis, M.S. Strano, J.N. Coleman, Liquid Exfoliation of Layered Materials, Science 340 (2013) 1226419, doi:10.1126/science.1226419.
[5] Y. Hernandez, V. Nicolosi, M. Lotya, F.M. Blighe, Z. Sun, S. De, T. McGovernI, B. Holland, M. Byrne, Y.K. Gun'Ko, J.J. Boland, P. Niraj, G. Duesberg, S. Krishnamurthy, R. Goodhue, J. Hutchison, V. Scardaci, A.C. Ferrari, J.N. Coleman, High-yield production of graphene by liquid-phase exfoliation of graphite, Nat Nano 3 (2008) 563–568.
[6] K.R. Paton, E. Varrla, C. Backes, R.J. Smith, U. Khan, Place A. O'Neill, C. Boland, M. Lotya, O.M. Istrate, P. King, T. Higgins, S. Barwich, P. May, P. Puczkarski, I. Ahmed, M. Moebius, H. Pettersson, E. Long, J. Coelho, S.E. O'Brien, E.K. McGuire, B.M. Sanchez, G.S. Duesberg, N. McEvoy, T.J. Pennycook, C. Downing, A. Crossley, V. Nicolosi, J.N. Coleman, Scalable production of large quantities of defect-free few-layer graphene by shear exfoliation in liquids, Nat. Mater. 13 (2014) 624–630.
[7] S. Park, R.S. Ruoff, Chemical methods for the production of graphenes, Nat. Nanotechnol. 4 (2009) 217–224, doi:10.1038/nnano.2009.58.
[8] W.S. Hummers, R.E. Offeman, Preparation of graphitic oxide, J. Am. Chem. Soc. 80 (1958) 1339, doi:10.1021/ja01539a017.
[9] S. Stankovich, D.A. Dikin, R.D. Piner, K.A. Kohlhaas, A. Kleinhammes, Y. Jia, Y. Wu, S.T. Nguyen, R.S. Ruoff, Synthesis of graphene-based nanosheets via chemical reduction of exfoliated graphite oxide, Carbon N Y 45 (2007) 1558–1565, doi:10.1016/j.carbon.2007.02.034.
[10] E. Varrla, K.R. Paton, C. Backes, A. Harvey, R.J. Smith, J. McCauley, J.N. Coleman, Turbulence-assisted shear exfoliation of graphene using household detergent and a kitchen blender, Nanoscale 6 (2014) 11810–11819, doi:10.1039/C4NR03560G.
[11] U. Khan, A. O'Neill, M. Lotya, S. De, J.N. Coleman, High-concentration solvent exfoliation of graphene, Small 6 (2010) 864–871, doi:10.1002/smll.200902066.
[12] X. Chen, J.F. Dobson, C.L. Raston, Vortex fluidic exfoliation of graphite and boron nitride, Chem. Commun. 48 (2012) 3703–3705, doi:10.1039/C2CC17611D.
[13] M. Lotya, P.J. King, U. Khan, S. De, J.N. Coleman, High-concentration, surfactant-stabilized graphene dispersions, ACS Nano 4 (2010) 3155–3162, doi:10.1021/nn1005304.
[14] R. Narayan, S.O. Kim, Surfactant mediated liquid phase exfoliation of graphene, Nano Convergence 2 (2015) 20, doi:10.1186/s40580-015-0050-x.
[15] Z. Sun, J. Masa, Z. Liu, W. Schuhmann, M. Muhler, Highly concentrated aqueous dispersions of graphene exfoliated by sodium taurodeoxycholate: dispersion behavior and potential application as a catalyst support for the oxygen-reduction reaction, Chem. – A Eur. J. 18 (2012) 6972–6978, doi:10.1002/chem.201103253.
[16] A.B. Bourlinos, V. Georgakilas, R. Zboril, T.A. Steriotis, A.K. Stubos, C. Trapalis, Aqueous-phase exfoliation of graphite in the presence of polyvinylpyrrolidone for the production of water-soluble graphenes, Solid State Commun. 149 (2009) 2172–2176, doi:10.1016/j.ssc.2009.09.018.
[17] D. Nuvoli, L. Valentini, V. Alzari, S. Scognamillo, S.B. Bon, M. Piccinini, J. Illescas, A. Mariani, High concentration few-layer graphene sheets obtained by liquid phase exfoliation of graphite in ionic liquid, J. Mater. Chem. 21 (2011) 3428–3431, doi:10.1039/C0JM02461A.
[18] S.M. Notley, Highly concentrated aqueous suspensions of graphene through ultrasonic exfoliation with continuous surfactant addition, Langmuir 28 (2012) 14110–14113, doi:10.1021/la302750e.
[19] C. Teng, D. Xie, J. Wang, Z. Yang, G. Ren, Y. Zhu, Ultrahigh conductive graphene paper based on ball-milling exfoliated graphene, Adv. Funct. Mater. 27 (2017) 1700240, doi:10.1002/adfm.201700240.
[20] H. Wu, W. Zhao, H. Hu, G. Chen, One-step in situball milling synthesis of polymer-functionalized graphene nanocomposites, J. Mater. Chem. 21 (2011) 8626–8632, doi:10.1039/C1JM10819K.
[21] P.G. Karagiannidis, S.A. Hodge, L. Lombardi, F. Tomarchio, N. Decorde, S. Milana, I. Goykhman, Y. Su, S.V. Mesite, D.N. Johnstone, R.K. Leary, P.A. Midgley, N.M. Pugno, F. Torrisi, A.C. Ferrari, Microfluidization of graphite and formulation of graphene-based conductive inks, ACS Nano 11 (2017) 2742–2755, doi:10.1021/acsnano.6b07735.
[22] F. Mori, M. Kubouchi, Y. Arao, Effect of graphite structures on the productivity and quality of few-layer graphene in liquid-phase exfoliation, J. Mater. Sci. 53 (2018) 12807–12815, doi:10.1007/s10853-018-2538-3.
[23] T.J. Nacken, C. Damm, J. Walter, A. Rüger, W. Peukert, Delamination of graphite in a high pressure homogenizer, RSC Adv. 5 (2015) 57328–57338, doi:10.1039/C5RA08643D.
[24] A. Amiri, M. Naraghi, G. Ahmadi, M. Soleymaniha, M. Shanbedi, A review on liquid-phase exfoliation for scalable production of pure graphene, wrinkled, crumpled and functionalized graphene and challenges, FlatChem 8 (2018) 40–71, doi:10.1016/j.flatc.2018.03.004.

[25] E. Varrla, C. Backes, K.R. Paton, A. Harvey, Z. Gholamvand, J. McCauley, J.N. Coleman, Large-scale production of size-controlled MoS2 nanosheets by shear exfoliation, Chem. Mater. 27 (2015) 1129–1139, doi:10.1021/cm5044864.
[26] X. Zhang, J. Xiang, C. Mu, F. Wen, S. Yuan, J. Zhao, D. Xu, C. Su, Z. Liu, SnS2 Nanoflakes anchored graphene obtained by liquid phase exfoliation and MoS2 nanosheet composites as lithium and sodium battery anodes, Electrochim. Acta 227 (2017) 203–209, doi:10.1016/j.electacta.2017.01.036.
[27] Z. Khanam, J. Liu, S. Song, Flexible graphene paper electrode prepared via polyvinyl alcohol-assisted shear-exfoliation for all-solid-state polymer supercapacitor application, Electrochim. Acta 363 (2020) 137208, doi:10.1016/j.electacta.2020.137208.
[28] S.S. Nemala, S. Ravulapalli, P. Kartikay, R. Banavath, S. Mallick, P. Bhargava, M. Bhushan, D. Mohapatra, Natural solvent facilitated high-shear exfoliated graphene nanoplatelets enabled economically-efficient and stable DSSC, Mater. Lett. 287 (2021) 129263, doi:10.1016/j.matlet.2020.129263.
[29] P. Zhou, Y. Liao, X. Yang, Y. Su, J. Yang, L. Xu, K. Wang, Z. Zeng, L. Zhou, Z. Zhang, Z. Su, Thermally stable, adhesively strong graphene/polyimide films for inkjet printing ultrasound sensors, Carbon N Y 184 (2021) 64–71, doi:10.1016/j.carbon.2021.08.007.
[30] A. Hajian, S.B. Lindström, T. Pettersson, M.M. Hamedi, L. Wågberg, Understanding the dispersive action of nanocellulose for carbon nanomaterials, Nano Lett. 17 (2017) 1439–1447, doi:10.1021/acs.nanolett.6b04405.
[31] P.M. Carrasco, S. Montes, I. García, M. Borghei, H. Jiang, I. Odriozola, G. Cabañero, V. Ruiz, High-concentration aqueous dispersions of graphene produced by exfoliation of graphite using cellulose nanocrystals, Carbon N Y 70 (2014) 157–163, doi:10.1016/j.carbon.2013.12.086.
[32] J.-M. Malho, P. Laaksonen, A. Walther, O. Ikkala, M.B. Linder, Facile method for stiff, tough, and strong nanocomposites by direct exfoliation of multilayered graphene into native nanocellulose matrix, Biomacromolecules 13 (2012) 1093–1099, doi:10.1021/bm2018189.
[33] J. Phiri, L.-S. Johansson, P. Gane, T.C. Maloney, Co-exfoliation and fabrication of graphene based microfibrillated cellulose composites – mechanical and thermal stability and functional conductive properties, Nanoscale 10 (2018) 9569–9582, doi:10.1039/C8NR02052C.
[34] W. Shao, S. Wang, H. Liu, J. Wu, R. Zhang, H. Min, M. Huang, Preparation of bacterial cellulose/graphene nanosheets composite films with enhanced mechanical performances, Carbohydr. Polym. 138 (2016) 166–171, doi:10.1016/j.carbpol.2015.11.033.
[35] X. Zhang, Z. Lu, J. Zhao, Q. Li, W. Zhang, C. Lu, Exfoliation/dispersion of low-temperature expandable graphite in nanocellulose matrix by wet co-milling, Carbohydr. Polym. 157 (2017) 1434–1441, doi:10.1016/j.carbpol.2016.11.023.
[36] Q. Jiang, C. Kacica, T. Soundappan, K. Liu, S. Tadepalli, P. Biswas, S. Singamaneni, An in situ grown bacterial nanocellulose/graphene oxide composite for flexible supercapacitors, J. Mater. Chem. A 5 (2017) 13976–13982, doi:10.1039/C7TA03824K.
[37] C. Yan, J. Wang, W. Kang, M. Cui, X. Wang, C.Y. Foo, K.J. Chee, P.S. Lee, Highly stretchable piezoresistive graphene–nanocellulose nanopaper for strain sensors, Adv. Mater. 26 (2014) 2022–2027, doi:10.1002/adma.201304742.
[38] A. Kafy, A. Akther, M.I.R. Shishir, H.C. Kim, Y. Yun, J. Kim, Cellulose nanocrystal/graphene oxide composite film as humidity sensor, Sensors Actuators A 247 (2016) 221–226, doi:10.1016/j.sna.2016.05.045.
[39] X. Xu, Y.-L. Hsieh, Aqueous exfoliated graphene by amphiphilic nanocellulose and its application in moisture-responsive foldable actuators, Nanoscale 11 (2019) 11719–11729, doi:10.1039/C9NR01602C.
[40] C. Ruiz-Palomero, S. Benítez-Martínez, M.L. Soriano, M. Valcárcel, Fluorescent nanocellulosic hydrogels based on graphene quantum dots for sensing laccase, Anal. Chim. Acta 974 (2017) 93–99, doi:10.1016/j.aca.2017.04.018.
[41] R. Arvidsson, B.A. Sandén, Carbon nanomaterials as potential substitutes for scarce metals, J. Clean. Prod. 156 (2017) 253–261, doi:10.1016/j.jclepro.2017.04.048.
[42] C. Cheng, S. Li, A. Thomas, N.A. Kotov, R. Haag, Functional graphene nanomaterials based architectures: biointeractions, fabrications, and emerging biological applications, Chem. Rev. 117 (2017) 1826–1914, doi:10.1021/acs.chemrev.6b00520.
[43] D. Bitounis, H. Ali-Boucetta, B.H. Hong, D.-H. Min, K. Kostarelos, Prospects and challenges of graphene in biomedical applications, Adv. Mater. 25 (2013) 2258–2268, doi:10.1002/adma.201203700.
[44] A.M. Pinto, I.C. Gonçalves, F.D. Magalhães, Graphene-based materials biocompatibility: a review, Colloids Surf. B 111 (2013) 188–202, doi:10.1016/j.colsurfb.2013.05.022.
[45] K.H. Wedepohl, The composition of the continental crust, Geochim. Cosmochim. Acta 59 (1995) 1217–1232, doi:10.1016/0016-7037(95)00038-2.
[46] S. Lund, J. Kauppila, S. Sirkiä, J. Palosaari, O. Eklund, R.-M. Latonen, J.-H. Smått, J. Peltonen, T. Lindfors, Fast high-shear exfoliation of natural flake graphite with temperature control and high yield, Carbon N Y 174 (2021) 123–131, doi:10.1016/j.carbon.2020.11.094.
[47] J.-W.T. Seo, A.A. Green, A.L. Antaris, M.C. Hersam, High-concentration aqueous dispersions of graphene using nonionic, biocompatible block copolymers, J. Phys. Chem. Lett. 2 (2011) 1004–1008, doi:10.1021/jz2003556.
[48] F.M. Smits, Measurement of sheet resistivities with the four-point probe, Bell Syst. Tech. J. 37 (1958) 711–718, doi:10.1002/j.1538-7305.1958.tb03883.x.
[49] J.K. Hoober, The Chlamydomonas Sourcebook. A Comprehensive Guide to Biology and Laboratory Use. Elizabeth H. Harris. Academic Press, San Diego, CA, 1989. xiv, 780 pp., illus. $145, Science (New York, N.Y.). 246 (1989) 1503–1504. https://doi.org/246/4936/1503-a [pii].
[50] R. Rippka, J. Deruelles, J.B. Waterbury, M. Herdman, Stanier, generic assignments, strain histories and properties of pure cultures of cyanobacteria, Microbiology 111 (1979) 1–61 (n.d.), doi:10.1099/00221287-111-1-1.
[51] H.K. Lichtenthaler, [34]Chlorophylls and carotenoids: pigments of photosynthetic biomembranes, Meth. Enzymol. 148 (1987) 350–382, doi:10.1016/0076-6879(87)48036-1.
[52] E. Touloupakis, B. Cicchi, G. Torzillo, A bioenergetic assessment of photosynthetic growth of Synechocystis sp. PCC 6803 in continuous cultures, Biotechnol. Biofuels 8 (2015) 133, doi:10.1186/s13068-015-0319-7.
[53] N.R. Baker, Chlorophyll fluorescence: a probe of photosynthesis in vivo, Annu. Rev. Plant Biol. 59 (2008) 89–113, doi:10.1146/annurev.arplant.59.032607.092759.
[54] T. Abitbol, E. Kloser, D.G. Gray, Estimation of the surface sulfur content of cellulose nanocrystals prepared by sulfuric acid hydrolysis, Cellulose 20 (2013) 785–794, doi:10.1007/s10570-013-9871-0.
[55] L. Chen, Q. Wang, K. Hirth, C. Baez, U.P. Agarwal, J.Y. Zhu, Tailoring the yield and characteristics of wood cellulose nanocrystals (CNC) using concentrated acid hydrolysis, Cellulose 22 (2015) 1753–1762, doi:10.1007/s10570-015-0615-1.
[56] N. Lin, A. Dufresne, Surface chemistry, morphological analysis and properties of cellulose nanocrystals with gradiented sulfation degrees, Nanoscale 6 (2014) 5384–5393, doi:10.1039/C3NR06761K.
[57] M.I. Voronova, O.V. Surov, A.G. Zakharov, Nanocrystalline cellulose with various contents of sulfate groups, Carbohydr. Polym. 98 (2013) 465–469, doi:10.1016/j.carbpol.2013.06.004.
[58] B. Sun, M. Zhang, Q. Hou, R. Liu, T. Wu, C. Si, Further characterization of cellulose nanocrystal (CNC) preparation from sulfuric acid hydrolysis of cotton fibers, Cellulose 23 (2016) 439–450, doi:10.1007/s10570-015-0803-z.
[59] X.M. Dong, J.-F. Revol, D.G. Gray, Effect of microcrystallite preparation conditions on the formation of colloid crystals of cellulose, Cellulose 5 (1998) 19–32, doi:10.1023/A:1009260511939.
[60] A.C. Ferrari, Raman spectroscopy of graphene and graphite: disorder, electron–phonon coupling, doping and nonadiabatic effects, Solid State Commun. 143 (2007) 47–57, doi:10.1016/j.ssc.2007.03.052.
[61] A.C. Ferrari, J.C. Meyer, V. Scardaci, C. Casiraghi, M. Lazzeri, F. Mauri, S. Piscanec, D. Jiang, K.S. Novoselov, S. Roth, A.K. Geim, Raman spectrum of graphene and graphene layers, Phys. Rev. Lett. 97 (2006) 187401, doi:10.1103/PhysRevLett.97.187401.
[62] L.M. Malard, M.A. Pimenta, G. Dresselhaus, M.S. Dresselhaus, Raman spectroscopy in graphene, Phys. Rep. 473 (2009) 51–87, doi:10.1016/j.physrep.2009.02.003.
[63] D. Yoon, H. Moon, H. Cheong, J. Choi, J. Choi, B. Park, Variations in the Raman spectrum as a function of the number of graphene layers, J. Korean Phys. Soc. 55 (2009) 1299–1303, doi:10.3938/jkps.55.1299.
[64] M.A. Pimenta, G. Dresselhaus, M.S. Dresselhaus, L.G. Cançado, A. Jorio, R. Saito, Studying disorder in graphite-based systems by Raman spectroscopy, Phys. Chem. Chem. Phys. 9 (2007) 1276–1290, doi:10.1039/B613962K.
[65] A. Eckmann, A. Felten, A. Mishchenko, L. Britnell, R. Krupke, K.S. Novoselov, C. Casiraghi, Probing the nature of defects in graphene by raman spectroscopy, Nano Lett. 12 (2012) 3925–3930, doi:10.1021/nl300901a.
[66] G.K.H. Pang, K.Z. Baba-Kishi, A. Patel, Topographic and phase-contrast imaging in atomic force microscopy, Ultramicroscopy 81 (2000) 35–40, doi:10.1016/S0304-3991(99)00164-3.
[67] R. Xiong, K. Hu, A.M. Grant, R. Ma, W. Xu, C. Lu, X. Zhang, V.V. Tsukruk, Ultrarobust transparent cellulose nanocrystal-graphene membranes with high electrical conductivity, Adv. Mater. 28 (2016) 1501–1509, doi:10.1002/adma.201504438.
[68] J. Phiri, L.-S. Johansson, P. Gane, T. Maloney, A comparative study of mechanical, thermal and electrical properties of graphene-, graphene oxide- and reduced graphene oxide-doped microfibrillated cellulose nanocomposites, Compos. Part B 147 (2018) 104–113, doi:10.1016/j.compositesb.2018.04.018.
[69] N.D. Luong, N. Pahimanolis, U. Hippi, J.T. Korhonen, J. Ruokolainen, L.-S. Johansson, J.-D. Nam, J. Seppälä, Graphene/cellulose nanocomposite paper with high electrical and mechanical performances, J. Mater. Chem. 21 (2011) 13991–13998, doi:10.1039/C1JM12134K.
[70] L.N. Dang, J. Seppälä, Electrically conductive nanocellulose/graphene composites exhibiting improved mechanical properties in high-moisture condition, Cellulose 22 (2015) 1799–1812, doi:10.1007/s10570-015-0622-2.
[71] E.B. Secor, M.H.D. Santos, S.G. Wallace, N.P. Bradshaw, M.C. Hersam, Tailoring the porosity and microstructure of printed graphene electrodes via polymer phase inversion, J. Phys. Chem. C 122 (2018) 13745–13750, doi:10.1021/acs.jpcc.8b00580.
[72] S. Barwich, J.M. de Araújo, A. Rafferty, C.G. da Rocha, M.S. Ferreira, J.N. Coleman, On the relationship between morphology and conductivity in nanosheet networks, Carbon N Y (2020), doi:10.1016/j.carbon.2020.09.015.
[73] J. Gong, J. Li, J. Xu, Z. Xiang, L. Mo, Research on cellulose nanocrystals produced from cellulose sources with various polymorphs, RSC Adv. 7 (2017) 33486–33493, doi:10.1039/C7RA06222B.
[74] A.D. French, Idealized powder diffraction patterns for cellulose polymorphs, Cellulose 21 (2014) 885–896, doi:10.1007/s10570-013-0030-4.
[75] Y. Nishiyama, J. Sugiyama, H. Chanzy, P. Langan, Crystal structure and hydrogen bonding system in cellulose iα from synchrotron X-ray and neutron fiber diffraction, J. Am. Chem. Soc. 125 (2003) 14300–14306, doi:10.1021/ja037055w.

[76] L. Segal, J.J. Creely, A.E. Martin, C.M. Conrad, An empirical method for estimating the degree of crystallinity of native cellulose using the X-ray diffractometer, Textile Res. J. 29 (1959) 786–794, doi:10.1177/004051755902901003.
[77] T. Zimmermann, E. Pöhler, T. Geiger, Cellulose fibrils for polymer reinforcement, Adv. Eng. Mater. 6 (2004) 754–761, doi:10.1002/adem.200400097.
[78] E. Tyystjärvi, Photoinhibition of Photosystem II and photodamage of the oxygen evolving manganese cluster, Coord. Chem. Rev. 252 (2008) 361–376, doi:10.1016/j.ccr.2007.08.021.
[79] L.T. Wey, P. Bombelli, X. Chen, J.M. Lawrence, C.M. Rabideau, S.J.L. Rowden, J.Z. Zhang, C.J. Howe, The development of biophotovoltaic systems for power generation and biological analysis, ChemElectroChem 6 (2019) 5375–5386, doi:10.1002/celc.201900997.
[80] J.Z. Zhang, P. Bombelli, K.P. Sokol, A. Fantuzzi, A.W. Rutherford, C.J. Howe, E. Reisner, Photoelectrochemistry of Photosystem II in Vitro vs in Vivo, J. Am. Chem. Soc. 140 (2018) 6–9, doi:10.1021/jacs.7b08563.